Title Page

(a) full article title
Crystal structure and reaction mechanism of a bacterial Mg-dechelatase homolog from the Chloroflexi *Anaerolineae*

(b) names and affiliations of all authors
Debayan Dey[1, 2], Masayoshi Nishijima[3], Ryouichi Tanaka[2], Genji Kurisu[3], Hideaki Tanaka[3], Hisashi Ito[2]
[1]Graduate School of Life Science, Hokkaido University, N10 W8, Sapporo 060-0810, Japan, [2]Institute of Low Temperature Science, Hokkaido University, N19 W8, Sapporo 060-0819, Japan
[3]Institute for Protein Research, Osaka University, Suita 565-0871, Osaka, Japan

(c) corresponding author
Hisashi Ito
Institute of Low Temperature Science, Hokkaido University, N19 W8, Sapporo 060-0819, Japan
E-mail: ito98@lowtem.hokudai.ac.jp
Tel: +81-11-706-5469
Fax: +81-11-706-5463

(d) running title
Bacterial Mg-dechelatase homolog characterization

(e) list of total number of manuscript pages, supplementary material pages, tables, and figures
Pages: 15
Supplementary material pages: 2
Tables: 2
Figures: 7

(f) a description of supplementary material including filenames.
Table S1. Primer sequences used for cloning and mutation
Figure S1. Photograph of AbSGR-h crystal and X-ray diffraction pattern.

Abstract

Chlorophyll degradation plays a myriad of physiological roles in photosynthetic organisms, including acclimation to light environment and nutrient remobilization during senescence. Mg extraction from chlorophyll *a* is the first and committed step of the chlorophyll degradation pathway. This reaction is catalyzed by the Mg-dechelatase enzyme encoded by *Stay-Green* (SGR). The reaction mechanism of SGR protein remains elusive since metal ion extraction from organic molecules is not a common enzymatic reaction. Additionally, experimentally derived structural information about SGR or its homologs has not yet been reported. In this study, the crystal structure of the SGR homolog from *Anaerolineae* bacterium was determined using the molecular replacement method at 1.85 Å resolution. Our previous study showed that three residues – H32, D34, and D62 are essential for the catalytic activity of the enzyme. Biochemical analysis involving mutants of D34 residue further strengthened its importance on the functioning of the dechelatase. Docking simulation also revealed interaction between the D34 side chain and central Mg ion of chlorophyll *a*. Structural analysis showed the arrangement of D34/H32/D62 in the form of a catalytic triad that is generally found in hydrolases. The probable reaction mechanism suggests that deprotonated D34 side chain coordinates and destabilizes Mg, resulting in Mg extraction. Besides, H32 possibly acts as a general base catalyst and D62 facilitates H32 to be a better proton acceptor. Taken together, the reaction mechanism of SGR partially mirrors the one observed in hydrolases.

Keywords

chlorophyll degradation, stay-green, Mg-dechelatase, crystal structure, catalytic triad

Statement

The first step of chlorophyll degradation during leaf senescence is catalyzed by Mg-dechelatase which extracts Mg from chlorophyll. The structural and biochemical analysis suggested a plausible reaction mechanism in which Mg is coordinated with the deprotonated aspartate side chain and extracted with the help of neighboring histidine and aspartate residues.

Abbreviations

βDDM, dodecyl β-maltoside; Chl, chlorophyll; SGR, Stay-Green; AbSGR-h, *Anaerolineae* bacterium SM23_63 SGR homolog; Mg-dechelatase, Magnesium-dechelatase

1, Introduction

Chlorophyll (Chl), the most abundant pigment on earth, is an indispensable molecule involved in the conversion of light energy and driving electron transfer during photosynthesis (1). Land plants and chlorophytes contain the two major types of chlorophyll – Chl *a* and *b* as protagonist molecules (2). In order to ensure efficient photosynthesis and other critical biological processes, maintenance of a balance in Chl metabolism becomes essential (3). Chl biosynthesis is important for effective photosynthetic performance during photosystem formation and adaptation to different environmental conditions (2). On the other hand, Chl degradation plays significant role in leaf senescence, fruit ripening, and seed maturation (4). Furthermore, Chl breakdown facilitates nutrient remobilization (5) and protects the plant against cellular photodamage (6). Therefore, both synthesis and degradation of Chl must be strictly regulated during the greening and senescence stages for ensuring plant viability.

The pathway of Chl degradation can be divided into: (1) a chloroplastic phase involving disassembly of the thylakoid leading to the opening of the tetrapyrrole ring of Chl and (2) a cytosolic and vacuolar phase that includes detoxification and sorting of the linear tetrapyrrole (4; 7). Prior to the initiation of Chl breakdown, Chl *b* must be converted to Chl *a* in a two-step enzymatic process called the Chl cycle (8; 9). This cycle is needed to finely regulate the Chl *a*/*b* ratio, a step important for acclimatizing plants to the light environment. Following conversion to Chl *a*, the pigment is eventually processed by four enzymes: (1) Mg-dechelatase (10); (2) pheophytinase acting as a dephytylase (11); (3) pheophorbide *a* oxygenase which catalyzes the irreversible opening of the porphyrin ring (12) to form the first linear tetrapyrrole (red chlorophyll catabolite) and (4) red chlorophyll catabolite reductase producing the primary fluorescent Chl catabolite which are then exported from chloroplasts and isomerized to non-fluorescent products by the acidic pH in the vacuole (13; 14). $C3^2$ of primary fluorescence catabolite can be hydroxylated before exporting from chloroplast (14).

The most important enzyme of the Chl degradation pathway is Mg-dechelatase encoded by the *Stay-Green* (SGR) gene, which is also responsible for Mendel's green cotyledon peas (15). It catalyzes the extraction of Mg from Chl *a* to form pheophytin *a* in a tightly regulated reaction so as to prevent the formation of damaging photosensitizing Chl metabolic intermediates (16; 10). Therefore, SGR not only catalyzes the most crucial and committed step of chlorophyll degradation but also removes a metal ion from an organic moiety in a biochemically enigmatic reaction. Apart from green plants (land plants and

green algae) and Glaucophytes, all other photosynthetic organisms like cyanobacteria and Rhodophyta lack SGR genes. On the other hand, SGR homologs are widely present in non-photosynthetic bacteria and Archaea. Further, Obata et al. demonstrated that bacterial SGR homolog with high Mg-dechelating activity was horizontally transferred to the ancestor of photosynthetic eukaryotes (17). Although high sequence similarity exists between SGR and its homologs, their catalytic activity and ligand specificity differ substantially among species (17). For instance, *Arabidopsis* SGR participate in Chl degradation whereas SGR in *Chlamydomonas reinhardtii* contributes to photosystem II formation (18). In addition to catalyzing the rate-limiting step of Chl breakdown, SGR plays a myriad of physiological roles in plant growth and (19), nodule senescence in legumes (20), fruit maturation (21) and regulation of the expression of genes encoding other chlorophyll degradation enzymes (22).

Although the biochemical reactions and key enzymes involved in the Chl metabolic pathway have been identified (10; 4), information on the structural aspects of these enzymes remain limited. In the Chl biosynthesis pathway after Mg insertion step, the crystal structures of Mg-chelatase and light dependent protochlorophyllide oxidoreductase have been elucidated, both of which catalyzes regulatory steps in the process (23-25). Among the enzymes participating in the four steps of Chl *a* conversion to primary fluorescent chlorophyll catabolite, the only crystal structure determined till now is of red chlorophyll catabolite reductase (26). We first reported the detailed structural characteristics of a bacterial SGR homolog from *Anaerolineae* bacterium SM23_63 (AbSGR-h) using a combination of computational and biochemical approaches (27). This bacterium belongs to Chloroflexi, which contain both photosynthetic organisms, green non-sulfur bacteria, and non-photosynthetic organisms. *Anaerolineae* bacterium SM23_63 is not a photosynthetic organism. Among all bacterial SGR homologs, we selected AbSGR-h because it is more evolutionarily related to land plant SGRs and overexpression of a soluble as well as active form of the protein is possible in *E. coli* using its general expression vector (17; 27).

There are two classes of enzyme involved in metal removal known to date – heme oxygenase and Mg-dechelatase (28; 10). The former enzyme cleaves a porphyrin ring to extract Fe^{2+} in a totally different mechanism from that of Mg-dechelatase (29). Therefore, this study not only proposes a novel reaction mechanism for Mg-dechelatase enzyme, but also provides the first crystal structure of a homolog from the SGR family. Furthermore, this study will become a basis for further studies on this enzyme, such as those for substrate specificity, screening for inhibitors and evolutionary analysis.

2, Results

2.1 Protein expression and purification

Our previous study have showed that three residues – H32, D34 and D62 in the AbSGR-h protein are critical for its catalytic activity, in which D34 is suggested to be involved in direct interaction with Chl *a* (27). Additionally, the presence of D34 on the surface of protein surrounded by a hydrophobic patch of residues, provides an ideal environment for interaction with the substrate. Since the main objective of this study is to delve deep into the reaction mechanism of Mg-dechelatase enzyme, three mutations on the aforementioned D34 residue were prepared to understand the effect of substitutions on the catalytic ability of AbSGR-h. D34 was changed to glutamate (D34E) to check whether replacement with a similar property amino acid altered the activity of AbSGR-h. It was also substituted with uncharged amino acids resulting in the formation of D34N and D34Q mutants. After expression of the wild-type and mutant SGRs in *E. coli*, the proteins were subjected to nickel column purification and subsequently to gel filtration analysis **(Figure 1)**. Histidine-tag was introduced into the N-terminal of recombinant protein for purification. Though histidine has affinity to metal ion and has a potential to affect enzymatic activity, interference by the tag in Mg extraction may be negligible because N-terminal does not localize near the active site in the structure as shown below.

According to a previous study, AbSGR-h was assumed to exist as a hexameric complex in solution (27). Major peaks were detected in the elution of gel filtration at the same position for the wild-type and three mutant AbSGR-h (D34E, D34N and D34Q), indicating the presence of the hexameric form of proteins. This observation further confirms the role of D34 to be mainly catalytic rather than maintaining the multimeric conformation of the protein. The molecular weight of the purified proteins was analyzed by SDS-PAGE **(Figure 2)**. Both wild-type and mutant proteins appeared as single and distinct bands corresponding to a molecular size of approximately 18 kDa. The stained gel also showed that the purity of these proteins was very high.

2.2 Mg-dechelating activity of SGR homolog

The Mg-dechelating activity of wild-type AbSGR-h and its mutants was tested *in vitro* using Chl *a* as the substrate. Enzymatic activity of AbSGR-h leads to the extraction of Mg^{2+} from Chl *a* to form pheophytin *a*. Activity levels were assessed based on the amounts of pheophytin *a* using HPLC **(Figure 3)**. An increase in the pheophytin peak on the HPLC profile is associated with the concomitant disappearance of the substrate Chl *a*. The wild-type protein exhibited the highest Mg-dechelating activity resulting in 1:1 chlorophyll to

pheophytin ratio in this profile. Interestingly, despite changing D34 with a similar kind of amino acid (Glu), the Mg-dechelating activity level of the mutant decreased substantially. The remaining mutations, *i.e.*, D34N and D34Q rendered the protein inactive in spite of being highly soluble, implying the potential role of this residue in catalysis.

2.3 Determination of kinetic parameter of SGR homolog

K_m and k_{cat} were determined for WT and D34E AbSGR-h with Mg-dechelating activity **(Figure 4)**. D34N and D34Q were inactive and hence not included in this assay. Purified proteins through nickel column and size exclusion chromatography were used. As D34E showed lower activity, a higher concentration (50 µM) of the recombinant protein was used compared with WT (5 µM). High concentrations of Chl *a* inhibited enzymatic activity, therefore the Michaelis-Menten curves were constructed with low Chl concentrations. The k_{cat} value of D34E (0.00035 min^{-1}) was significantly lower than that of WT (0.076 min^{-1}), suggesting that D34 is involved in catalysis. Though K_m value of D34E (6.00 µM) was lower than that of WT (15.91 µM), the difference was not so pronounced as that of k_{cat} **(Table 1)**.

2.4 Crystal structure of AbSGR-h

The crystal structure of AbSGR-h was determined using the molecular replacement method at 1.85 Å resolution **(Figure S1)**. Owing to the lack of homologous templates with SGR, the AlphaFold2 predicted structure of rice SGR (UniProt: Q652K1) was used as a starting model. The crystallographic data and refinement statistics are provided in **Table 2**.

The X-ray crystal structure shows two SGR molecules in the asymmetric unit **(Figure 5a)**. Each monomeric structure comprises two α-helices, four 3-10 helices, and seven β-strands, as revealed by STRIDE analysis **(Figure 5b)**. The β-strands constitute one β-sheet leading to the formation of a curved structure, inside which the larger α-helix (residues 92 – 120) is accommodated. These observations are almost in accordance with the secondary structure architecture of the computationally predicted structure of AbSGR-h (27). The root mean square deviation, based on Cα-atoms, between the crystal and computationally predicted structure is 1.28 Å, where the difference remains restricted to the loop regions of the two structures.

2.5 Substrate docking analysis

Molecular docking analysis considering energy-minimized free Chl *a* as the substrate was

carried out in AutoDock Vina. The actual substrate of SGR *in vivo* is Chl *a* bound to chlorophyll-protein complexes that are embedded in the thylakoid membrane (30). The grid box was set around the active site of the protein such that it covers three residues – H32, D34 and D62, all of which are catalytically important (27). The docking analysis revealed interaction of the central Mg ion of Chl *a* with the carbonyl oxygen atom of D34 residue in the crystal structure of AbSGR-h monomer **(Figure 6a, Supplementary File 1)**. The distance between the aforementioned atoms was found to be ~ 4.4 Å. The interaction between the two moieties was stable, as indicated from the binding affinity value (-7.8 kcal/mol).

3, Discussion

3.1 Comparison of the crystal structure with the computationally predicted structure

In this study, the crystal structure of AbSGR-h was determined using the molecular replacement method at 1.85 Å resolution. The crystal and computationally predicted structure were found to be almost identical. In our previous study, mutation in R26, Y28, T29, and D114 rendered the recombinant protein insoluble, suggesting that these residues are essential for maintaining the AbSGR-h structure form (27). The positions of these residues were correctly predicted in the computationally derived structure. However, the arrangements of the active site were slightly different **(Figure 7)**. The turn between the 2nd and 3rd β-sheet was not tightly packed in the crystal structure. Thus, H32 and D34 residing in this region are more flexible than those in the computationally predicted structure. In fact, this result is in agreement with the previous study where root mean square fluctuation for individual residues obtained by molecular dynamics simulation showed that the site of D34 is flexible (27). Although H32 and D34 positions were slightly different, the Cα-atoms of D62 were found in the same position for both the structures. However, the orientation of the side chains of D62 was different. In the crystal structure, the side chain faces outwards, which facilitate interaction of this side chain with that of H32. Although minor differences exist in the active site arrangement as compared to the computationally predicted structure, the relatively more flexibility of the same in crystal structure hints at the high accuracy of X-ray crystallography in the field of protein structure derivation.

3.2 Enzymatic properties of AbSGR-h

The kinetic parameters of AbSGR-h were examined in this study where K_m was found to be 15.91 µM. This is in concordance with the reported values of plant, green algae and bacterial recombinant proteins (17). Pheophytinase and pheophorbide *a* oxygenase catalyze

the successive reactions of SGR. K_m values of the recombinant proteins of *Arabidopsis* pheophytinase and pheophorbide *a* oxygenase were 14.35 µM and 6.0 µM, respectively (12; 31). These enzymes, involved in chlorophyll breakdown pathway, have similar substrate affinities. When D34 in AbSGR-h was substituted by glutamate, the K_m was 6.0 µM. This substitution did not have negative effect on the affinity of ligand to the protein, suggesting that D34 is indispensable for the activity but does not play a major role in the determination of substrate specificity. k_{cat} of AbSGR-h was 0.076 in 1 min. Physiologically, this catalytic rate is too low. It may be assumed that chlorophylls as chlorophyll-protein complexes are better substrate for SGR. Chlorophyll solubilized with detergent is under different conditions from that of native chlorophyll within chloroplasts. Low reaction rates of the recombinant protein have also been reported in the bacteriochlorophyll anabolic pathway (32) and the cyanobacterial chlorophyll catabolic pathway (33). k_{cat} of D34E was 0.00035 in 1 min, which is much lower than that of WT AbSGR-h. D34N and D34Q resulted in inactivation of the enzyme. All these four recombinant proteins showed the same profiles in gel filtration, suggesting that mutation in D34 does not affect the quaternary structure. These observations suggest that the carboxyl group of this acidic amino acid residue is indispensable for activity and SGR is optimized to use aspartate for the reaction.

3.3 Proposed reaction mechanism of SGR

In a previous study, a multiple sequence alignment of SGR showed that H32, D34 and D62 residues are conserved among SGR homologs (27). These three amino acids were found to be essential for the enzymatic activity **(Figure 7)** and docking simulation also suggested that D34 interacts with Chl *a* **(Figure 6a)**. Additionally, these residues were close together in the tertiary structure of AbSGR-h. The observations, herein, show striking resemblance with the catalytic triad found in hydrolases, which is usually composed of serine, histidine and aspartate residues with similar spatial arrangements including some variations (34). In case of the catalytic triad of chymotrypsin, the side chain of S195 is polarized and deprotonated with the support of H57 (35; 36), while D102 is involved in the charge-relay mechanism. AbSGR-h has aspartate in the active site instead of serine. The distance between D34 side chain and H32 side chain is 3.5 Å and that between H32 side chain and D62 side chain is 2.6 Å **(Figure 6a)**. In the catalytic triad of chymotrypsin (PDB accession: 1AFQ) the distance between S195 – H57 side chains and H57 – D102 side chains are both 2.8 Å **(Figure 6b)**. Though the distance between D34 – H32 side chains (3.5 Å) in AbSGR-h is longer than that between S195 and H57 (2.8 Å) of chymotrypsin, it is short enough to form a hydrogen bond. Perhaps, H32 of AbSGR-h probably does not need to act as a base catalyst as strongly as H57 of chymotrypsin, because the aspartate carboxyl group is readily

deprotonated than the serine hydroxyl group. These observations suggest that D34, H32 and D62 are arranged in the form of a catalytic triad to deprotonate D34 side chain, which is exposed to the aqueous environment and may be deprotonated easily. The deprotonated side chain of D34 may coordinate stably with Mg of chlorophyll, which probably destabilizes Mg-tetrapyrrole ring interaction, resulting in extraction of Mg from chlorophyll. Two protons replaced with Mg will be supplied from the stromal solution. This forms a plausible reaction mechanism of SGR, which needs to be tested experimentally.

When we investigate the catalytic mechanism of SGR, another likely scenario may be that D34 and D62 side chains function as an acid catalyst by donating protons to nitrogen of pyrroles coordinating Mg, resulting in exchange of Mg with protons to produce pheophytin. In this case, H32 coordinates Mg. This assumed reaction is similar to Mg extraction observed under the acidic conditions. However, it is not likely in case of SGR. Acidic amino acid side chain can function as the acid catalyst as found in the lysozyme glutamate (37). Lysozyme glutamate is present in a protonated form because of localization in the hydrophobic environment, which is essential to keep the protonated form of the acidic amino acid residues. Though D62 localizes in the hydrophobic cavity of the active site, D34 of AbSGR-h stays in a hydrophilic environment and thus may not be able to act as the acidic catalyst. Altogether, protein structure and enzymatic analysis suggest that SGR removes Mg by coordinating with the deprotonated side chain of aspartate and destabilizing the bond between Mg and pyrrole nitrogen. Co-crystallization of SGR with the pigment is necessary for verifying this predicted reaction mechanism in future.

4, Conclusion

SGR catalyzes Mg extraction from chlorophyll in a biochemically inexplicable enzymatic reaction where a metal ion is extracted from an organic molecule. In this study, we proposed the reaction mechanism of this enzyme based on biochemical and crystal structure analysis. Side chain of the acidic amino acid residue, D34, possibly coordinates with Mg of chlorophyll and destabilizes it. H32 acts as the base catalyst by accepting the hydrogen from D34 whereas D62 makes H32 a better proton acceptor through electrostatic effects. The arrangement of these amino acid residues is similar to the catalytic triad generally found in hydrolases. The structure of the active site was slightly different from the computationally predicted structure in terms of side chain orientations and inter-residue distances. The crystal structure revealed a more open and flexible active site when compared to the computationally predicted structure. Nevertheless, SGR co-crystallized with chlorophyll will promote better understanding of the enzyme mechanism, which leaves ample scope for future studies.

5, Materials and methods

5.1 Cloning of bacterial SGR homolog

Bacterial SGR homolog from *Anaerolineae* bacterium SM23_63 (AbSGR-h) encoded by KPK94580 with optimized codon usage for *E. coli* was artificially synthesized according to a previously reported protocol (17). AbSGR-h was amplified from the artificially synthesized DNA using the primer sets provided in **Table S1**. PCR amplified DNA fragments were cloned into pET 30a (+) vectors (Novagen) containing a histidine-tag at the C-terminus using the *Nde*I and *Xho*I sites through an in-fusion cloning system (Clontech). Point mutations were introduced by PCR using primers as shown in **Table S1**.

5.2 Expression, detection and purification of recombinant proteins

The constructed plasmids for protein expression were introduced into *E. coli* BL21 (DE3). *E. coli* was grown and an auto-induction medium (6 g Na_2HPO_4, 3 g KH_2PO_4, 20 g tryptone, 5 g yeast extract, 5 g NaCl, 6 mL glycerol, 0.5 g glucose, 2 g lactose, 100 mg kanamycin in 1L) at 37ºC for 16 h with 120 rpm shaking was used for expression of the recombinant protein (38). After induction of the recombinant protein, 200 mL of culture cells were harvested by centrifugation at 7,000 g for 5 min. The harvested cells were resuspended in buffer A (20 mM Na-phosphate pH 7.4, 100 mM NaCl, 20 mM imidazole) and disrupted by sonication (Branson Sonifier SFX250: output 8, duty cycle 20%) for 6 min in an ice bath. After sonication, dodecyl β-maltoside (βDDM) was added to the final concentration of 0.05% (w/v) and incubated for 5 min at 25ºC. The cleared supernatant of cell lysate was obtained by centrifugation at 15,000 g for 20 min in 4ºC and then loaded onto a 5 mL HisTrap HP column (Cytiva) equilibrated with buffer A containing 0.05% βDDM using an ÄKTAprime plus system (Cytiva). The recombinant proteins were eluted by buffer B (20 mM Na-phosphate pH 7.4, 100 mM NaCl, 500 mM imidazole, 0.05% βDDM). The purified protein was further analyzed by size exclusion chromatography using Sephacryl S-300 HR (Cytiva) equilibrated with buffer C (20 mM Na-phosphate pH 7.4, 100 mM NaCl, 0.05% βDDM). The protein elution profile was monitored by absorbance at 280 nm. The molecular weight of AbSGR-h was evaluated by comparison to protein standards (Gel Filtration Calibration Kit LMW, Cytiva) as previously reported (27). To examine the purity of the protein, elution was mixed with the same volume of the sample buffer containing 125 mM Tris- HCl, pH 6.8, 4% (w/v) SDS, 10% (w/v) sucrose, and 5% (v/v) 2-mercaptoethanol. Mixtures were incubated at 95ºC for 1 min and 1 μg of protein was used for SDS-PAGE followed by staining with Coomassie Brilliant Blue for visualization. Protein concentration in the purified solution was quantified using the Bradford protein

assay using bovine serum albumin as a standard.

5.3 Activity assay

Activity assays were performed with Chl *a* dissolved in dimethyl sulfoxide and at a final dimethyl sulfoxide concentration of 2% (v/v) in the reaction mixture. Purified recombinant proteins (50 μM) were incubated with Chl *a* (20 μM) for 10 min at 25°C in 50 μL of the reaction buffer comprising 20 mM Na-phosphate pH 7.4, 100 mM NaCl, 0.05% βDDM. Reactions were stopped by adding 200 μL of acetone, followed by centrifugation at 20,000 g for 10 min. Reactions were analyzed by HPLC as previously reported (27). To determine kinetic parameter, Chl *a* at different concentrations (2.5, 5, 10, 20 μM) was incubated with WT (5 μM) or D34E (50 μM) for 20 min. Three samples were used for each concentration. The Michaelis-Menten curves were calculated by the least-squares method using Microsoft Excel Solver (Microsoft).

5.4 Crystallization

After removal of detergent using a desalting column (PD-10, Cytiva), crystals of SGR were obtained by sitting-drop vapor diffusion method at 25°C. A sitting drop was prepared by mixing equal volumes of AbSGR-h solution and reservoir solution containing 100 mM Tris-HCl (pH 8.5), 200 mM ammonium phosphate monobasic and 50% (v/v) 2-methyl-2,4-pentanediol (Crystal Screen Kit II No. 43, Hampton Research). The initial crystals appeared for two days, and in the 1-2 weeks, these crystals grew to as large as 0.1 mm in their longest dimensions. Since the reservoir solution contained 50% (v/v) 2-Methyl-2,4-pentanediol, the crystals were picked up directly from the sitting drop and immediately frozen in liquid nitrogen. This crystal diffracted up to 1.85 Å resolution and belonged to space group $P6_122$ with cell dimensions of a=80.3 Å, b=80.3 Å, c=224.8 Å, β=120.0°.

5.5 X-ray intensity data collection and structure determination

X-ray intensity data was collected on BL44XU at SPring-8 (Harima, Hyogo, Japan) using EIGER X16M detector (Dectris) at cryogenic temperature (100 K). The diffraction data were processed and scaled using the program XDS (39). The initial phase was determined by the molecular replacement method with the program PHASER in CCP4 (40) using the AlphaFold2 predicted structure of rice SGR (UniProt: Q652K1) as a starting model. The structure model was manually built using the program COOT (41) in CCP4, and refinement was performed using phenix refine (42) in PHENIX. Secondary structure assignment was implemented using the STRIDE web-server (43). All figures showing the atomic

coordinates were made with PyMOL (The PyMOL Molecular Graphics System, Version 2.0 Schrödinger, LLC.).

5.6 Substrate docking analysis

The KEGG LIGAND database (https://www.genome.jp/kegg/ligand.html) was used for retrieving the structure of Chl *a*. It was then subjected to geometry optimization under the semiempirical method in HyperChemTM 8.0.8 molecular modeling software (Hypercube). Steepest descent followed by the Polak-Ribiere conjugate gradient algorithm was performed for energy optimization of Chl *a* until convergence was reached. Open Babel was used for the interconversion of structures with different file formats (44). Protein-ligand docking study was carried out using AutoDock Vina v1.1.2 considering chain A of the crystal structure of wild-type AbSGR-h (45). The pre-docking parameters were set using AutoDock Tools v4 with the addition of polar hydrogen atoms and Gasteiger charges to the protein molecule (46). A grid box of 30 Å × 30 Å × 30 Å with grid spacing of 1 Å was set and no solvation was considered for the docking procedure. Interactions in the docked conformations were visualized using PyMOL.

Acknowledgments

We would like to thank Prof. Hideaki Ogata, University of Hyogo, for helpful discussion. This work was performed in part under the Collaborative Research Program of Institute for Protein Research, Osaka University, CR -22-02.

Figure Legends

Figure 1 Size exclusion chromatography profiles of AbSGR-h and its mutants. Protein was monitored by the absorbance at 280 nm. Protein markers with known molecular weights are also shown.

Figure 2 Analysis of purity and molecular weight of purified WT and mutated AbSGR-h proteins. Purified proteins by size exclusion chromatography were separated by SDS-PAGE and stained.

Figure 3 Examination of activity of AbSGR-h. Chl *a* was incubated with gel filtration derived purified proteins of wild-type or mutant AbSGR-h. After incubation, pigments were extracted and analyzed by HPLC. Chl *a* and pheophytin *a* peaks are also shown.

Figure 4 Michaelis-Menten analysis of WT and D34E mutant AbSGR-h protein. Different concentrations (2.5, 5, 10, 20) of Chl *a* was incubated with WT (5 µM) or D34E (50 µM) for 20 min and the accumulation of pheophytin *a* was monitored by HPLC.

Figure 5 Overall structure of the AbSGR-h protein. (a) Cartoon representation of the AbSGR-h dimer (PDB ID: 7Y5Y) showing chain A (green) and chain B (blue). (b) Secondary structure assignment of AbSGR-h with STRIDE. Red and blue helix shows α-helices and 3-10 helices, respectively. Green arrows indicate β-strands.

Figure 6 Structure of AbSGR-h and chymotrypsin. Molecular docking analysis of Chl *a* with the crystal structure of AbSGR-h monomer was performed in AutoDock Vina (a). Also, the residues constituting the catalytic triad along with the distance between them for (a) AbSGR-h and (b) chymotrypsin have been shown.

Figure 7 Structural superimposition of the crystal (green) and computationally predicted structure (orange) of AbSGR-h protein. Side chain of H32, D34 and D62 residues for crystal and predicted structure are colored in red and blue, respectively.

References

1. Hörtensteiner S (2009) Stay-green regulates chlorophyll and chlorophyll-binding protein degradation during senescence. Trends Plant Sci 14:155-162.
2. Tanaka R, Tanaka A (2007) Tetrapyrrole Biosynthesis in Higher Plants. Annu Rev Plant Biol 58:321-346.

3. Mochizuki N, Tanaka R, Grimm B, Masuda T, Moulin M, Smith AG, Tanaka A, Terry MJ (2010) The cell biology of tetrapyrroles: a life and death struggle. Trends Plant Sci 15:488-498.
4. Kuai B, Chen J, Hörtensteiner S (2018) The biochemistry and molecular biology of chlorophyll breakdown. J Exp Bot 69:751-767.
5. vom Dorp K, Hölzl G, Plohmann C, Eisenhut M, Abraham M, Weber APM, Hanson AD, Dörmann P (2015) Remobilization of Phytol from Chlorophyll Degradation Is Essential for Tocopherol Synthesis and Growth of Arabidopsis. Plant Cell 27:2846-2859.
6. Hörtensteiner S, Krautler B (2011) Chlorophyll breakdown in higher plants. Biochim Biophys Acta 1807:977-988.
7. Schumacher I, Menghini D, Ovinnikov S, Hauenstein M, Fankhauser N, Zipfel C, Hörtensteiner S, Aubry S (2022) Evolution of chlorophyll degradation is associated with plant transition to land. Plant J 109:1473-1488.
8. Sato Y, Morita R, Katsuma S, Nishimura M, Tanaka A, Kusaba M (2009) Two short-chain dehydrogenase/reductases, NON-YELLOW COLORING 1 and NYC1-LIKE, are required for chlorophyll b and light-harvesting complex II degradation during senescence in rice. Plant J 57:120-131.
9. Meguro M, Ito H, Takabayashi A, Tanaka R, Tanaka A (2011) Identification of the 7-hydroxymethyl chlorophyll a reductase of the chlorophyll cycle in Arabidopsis. Plant Cell 23:3442-3453.
10. Shimoda Y, Ito H, Tanaka A (2016) Arabidopsis STAY-GREEN, Mendel's green cotyledon gene, encodes magnesium-dechelatase. Plant Cell 28:2147-2160.
11. Schelbert S, Aubry S, Burla B, Agne B, Kessler F, Krupinska K, Hörtensteiner S (2009) Pheophytin pheophorbide hydrolase (pheophytinase) is involved in chlorophyll breakdown during leaf senescence in Arabidopsis. Plant Cell 21:767-785.
12. Pruzinska A, Tanner G, Anders I, Roca M, Hörtensteiner S (2003) Chlorophyll breakdown: pheophorbide a oxygenase is a Rieske-type iron-sulfur protein, encoded by the accelerated cell death 1 gene. Proc Natl Acad Sci U S A 100:15259-15264.
13. Pruzinska A, Anders I, Aubry S, Schenk N, Tapernoux-Luthi E, Muller T, Krautler B, Hörtensteiner S (2007) In vivo participation of red chlorophyll catabolite reductase in chlorophyll breakdown. Plant Cell 19:369-387.
14. Hauenstein M, Christ B, Das A, Aubry S, Hörtensteiner S (2016) A Role for TIC55 as a Hydroxylase of Phyllobilins, the Products of Chlorophyll Breakdown during Plant Senescence. Plant Cell 28:2510-2527.
15. Sato Y, Morita R, Nishimura M, Yamaguchi H, Kusaba M (2007) Mendel's green cotyledon gene encodes a positive regulator of the chlorophyll-degrading pathway. Proc Natl Acad Sci U S A 104:14169-14174.
16. Hirashima M, Tanaka R, Tanaka A (2009) Light-independent cell death induced by accumulation of pheophorbide a in Arabidopsis thaliana. Plant Cell Physiol 50:719-729.
17. Obata D, Takabayashi A, Tanaka R, Tanaka A, Ito H (2019) Horizontal Transfer of Promiscuous Activity from Nonphotosynthetic Bacteria Contributed to Evolution of Chlorophyll Degradation Pathway. Mol Biol Evol 36:2830-2841.
18. Chen Y, Shimoda Y, Yokono M, Ito H, Tanaka A (2019) Mg-dechelatase is involved in the formation of photosystem II but not in chlorophyll degradation in Chlamydomonas reinhardtii. Plant J 97:1022-1031.

19. Delmas F, Sankaranarayanan S, Deb S, Widdup E, Bournonville C, Bollier N, Northey JGB, McCourt P, Samuel MA (2013) ABI3 controls embryo degreening through Mendel's I locus. Proc Natl Acad Sci U S A 110:E3888-E3894.
20. Zhou C, Han L, Pislariu C, Nakashima J, Fu C, Jiang Q, Quan L, Blancaflor EB, Tang Y, Bouton JH, Udvardi M, Xia G, Wang Z-Y (2011) From Model to Crop: Functional Analysis of a STAY-GREEN Gene in the Model Legume Medicago truncatula and Effective Use of the Gene for Alfalfa Improvement. Plant Physiol 157:1483-1496.
21. Luo Z, Zhang J, Li J, Yang C, Wang T, Ouyang B, Li H, Giovannoni J, Ye Z (2013) A STAY-GREEN protein SlSGR1 regulates lycopene and β-carotene accumulation by interacting directly with SlPSY1 during ripening processes in tomato. New Phytol 198:442-452.
22. Sato T, Shimoda Y, Matsuda K, Tanaka A, Ito H (2018) Mg-dechelation of chlorophyll a by Stay-Green activates chlorophyll b degradation through expressing Non-Yellow Coloring 1 in Arabidopsis thaliana. J Plant Physiol 222:94-102.
23. Zhang S, Heyes DJ, Feng L, Sun W, Johannissen LO, Liu H, Levy CW, Li X, Yang J, Yu X, Lin M, Hardman SJO, Hoeven R, Sakuma M, Hay S, Leys D, Rao Z, Zhou A, Cheng Q, Scrutton NS (2019) Structural basis for enzymatic photocatalysis in chlorophyll biosynthesis. Nature 574:722-725.
24. Adams NBP, Bisson C, Brindley AA, Farmer DA, Davison PA, Reid JD, Hunter CN (2020) The active site of magnesium chelatase. Nature Plants 6:1491-1502.
25. Bryant DA, Hunter CN, Warren MJ (2020) Biosynthesis of the modified tetrapyrroles-the pigments of life. J Biol Chem 295:6888-6925.
26. Sugishima M, Okamoto Y, Noguchi M, Kohchi T, Tamiaki H, Fukuyama K (2010) Crystal Structures of the Substrate-Bound Forms of Red Chlorophyll Catabolite Reductase: Implications for Site-Specific and Stereospecific Reaction. J Mol Biol 402:879-891.
27. Dey D, Dhar D, Fortunato H, Obata D, Tanaka A, Tanaka R, Basu S, Ito H (2021) Insights into the structure and function of the rate-limiting enzyme of chlorophyll degradation through analysis of a bacterial Mg-dechelatase homolog. Comput Struct Biotechnol J 19:5333-5347.
28. Yoshida T, Migita CT (2000) Mechanism of heme degradation by heme oxygenase. J Inorg Biochem 82:33-41.
29. Unno M, Matsui T, Ikeda-Saito M (2007) Structure and catalytic mechanism of heme oxygenase. Nat Prod Rep 24:553-570.
30. Nelson N, Yocum CF (2006) Structure and function of photosystems I and II. Annu Rev Plant Biol 57:521-565.
31. Guyer L, Salinger K, Krügel U, Hörtensteiner S (2018) Catalytic and structural properties of pheophytinase, the phytol esterase involved in chlorophyll breakdown. J Exp Bot 69:879-889.
32. Nomata J, Swem LR, Bauer CE, Fujita Y (2005) Overexpression and characterization of dark-operative protochlorophyllide reductase from Rhodobacter capsulatus. Biochim Biophys Acta 1708:229-237.
33. Takatani N, Uenosono M, Hara Y, Yamakawa H, Fujita Y, Omata T (2022) Chlorophyll and Pheophytin Dephytylating Enzymes Required for Efficient Repair of PSII in Synechococcus elongatus PCC 7942. Plant Cell Physiol 63:410-420.
34. Ekici OD, Paetzel M, Dalbey RE (2008) Unconventional serine proteases: variations on the catalytic Ser/His/Asp triad configuration. Protein Sci 17:2023-2037.

35. Derewenda ZS, Derewenda U, Kobos PM (1994) (His)Cε-H···O=C< Hydrogen Bond in the Active Sites of Serine Hydrolases. J Mol Biol 241:83-93.
36. Frey PA, Whitt SA, Tobin JB (1994) A Low-Barrier Hydrogen Bond in the Catalytic Triad of Serine Proteases. Science 264:1927-1930.
37. Malcolm BA, Rosenberg S, Corey MJ, Allen JS, Baetselier Ad, Kirsch JF (1989) Site-directed mutagenesis of the catalytic residues Asp-52 and Glu-35 of chicken egg white lysozyme. Proc Natl Acad Sci U S A 86:133-137.
38. Studier FW (2005) Protein production by auto-induction in high density shaking cultures. Protein Expr Purif 41:207-234.
39. Kabsch W (2010) XDS. Acta Crystallogr D 66:125-132.
40. McCoy AJ, Grosse-Kunstleve RW, Adams PD, Winn MD, Storoni LC, Read RJ (2007) Phaser crystallographic software. J Appl Crystallogr 40:658-674.
41. Emsley P, Cowtan K (2004) Coot: model-building tools for molecular graphics. Acta Crystallogr D 60:2126-2132.
42. Liebschner D, Afonine PV, Baker ML, Bunkoczi G, Chen VB, Croll TI, Hintze B, Hung L-W, Jain S, McCoy AJ, Moriarty NW, Oeffner RD, Poon BK, Prisant MG, Read RJ, Richardson JS, Richardson DC, Sammito MD, Sobolev OV, Stockwell DH, Terwilliger TC, Urzhumtsev AG, Videau LL, Williams CJ, Adams PD (2019) Macromolecular structure determination using X-rays, neutrons and electrons: recent developments in Phenix. Acta Crystallogr D 75:861-877.
43. Heinig M, Frishman D (2004) STRIDE: a web server for secondary structure assignment from known atomic coordinates of proteins. Nucleic Acids Res 32:W500-W502.
44. O'Boyle NM, Banck M, James CA, Morley C, Vandermeersch T, Hutchison GR (2011) Open Babel: An open chemical toolbox. J Cheminform 3:33.
45. Trott O, Olson AJ (2010) AutoDock Vina: improving the speed and accuracy of docking with a new scoring function, efficient optimization, and multithreading. J Comput Chem 31:455-461.
46. Morris GM, Huey R, Lindstrom W, Sanner MF, Belew RK, Goodsell DS, Olson AJ (2009) AutoDock4 and AutoDockTools4: Automated docking with selective receptor flexibility. J Comput Chem 30:2785-2791.

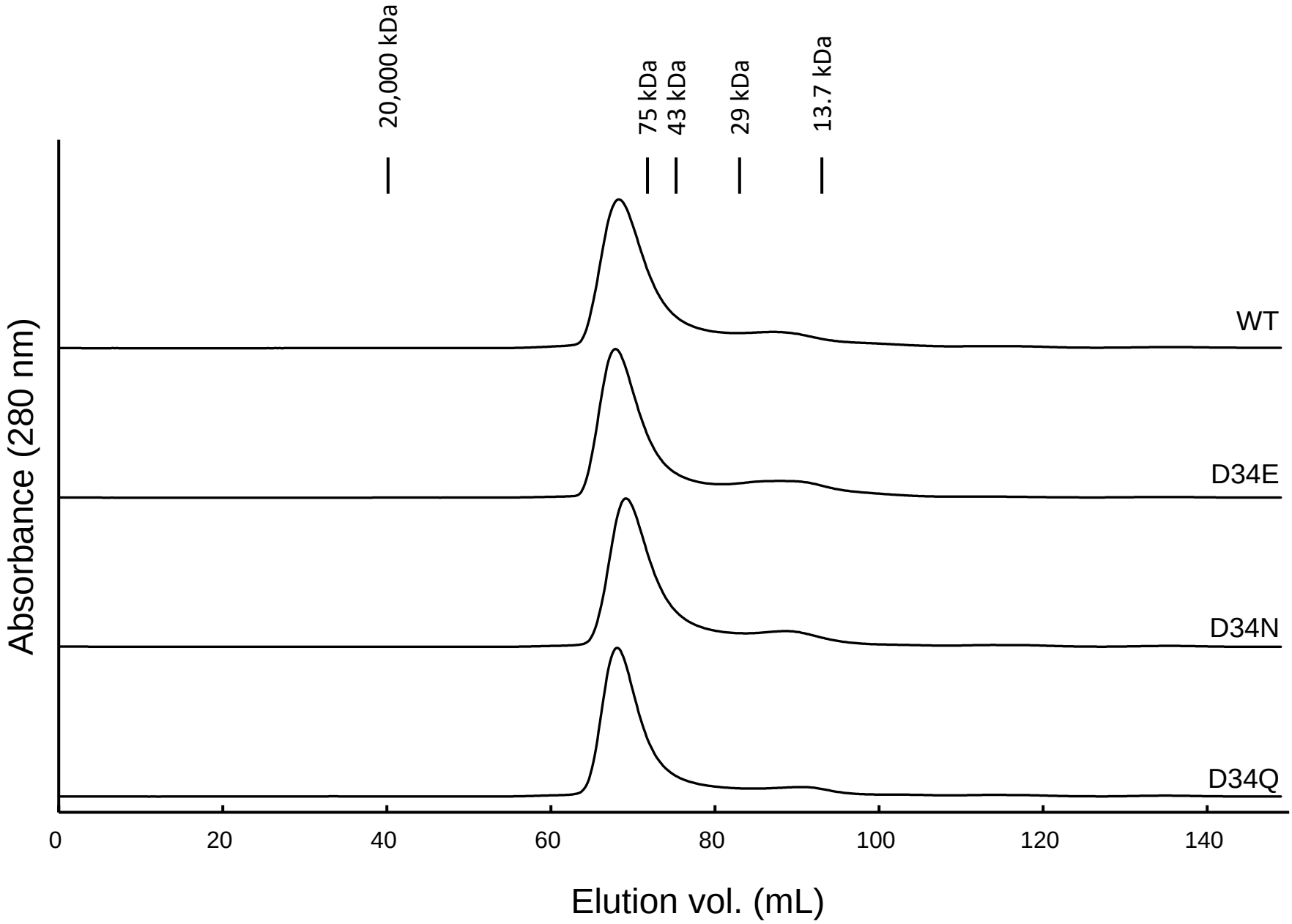
20,000 kDa
75 kDa
43 kDa
29 kDa
13.7 kDa
WT
D34E
D34N
D34Q
Absorbance (280 nm)
0
20
40
60
80
100
120
140
Elution vol. (mL)

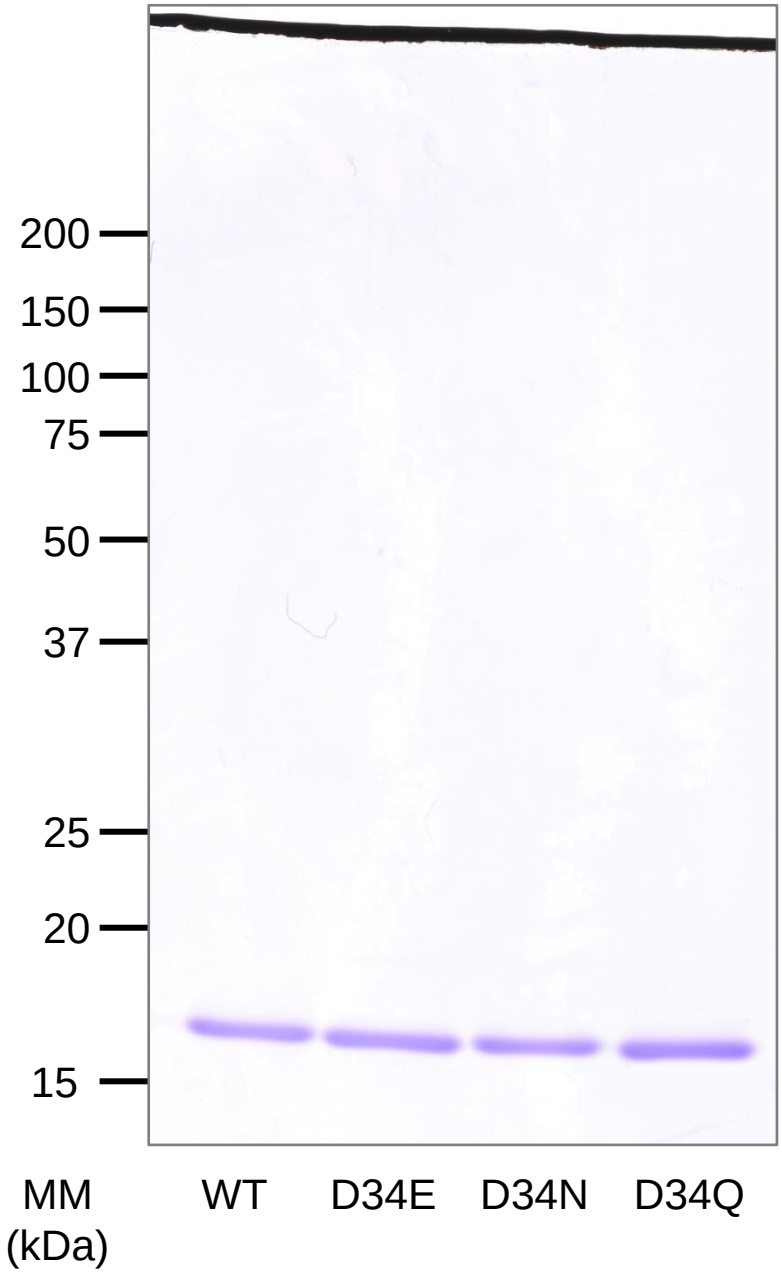
200
150
100
75
50
37
25
20
15
MM
(kDa)
WT
D34E
D34N
D34Q

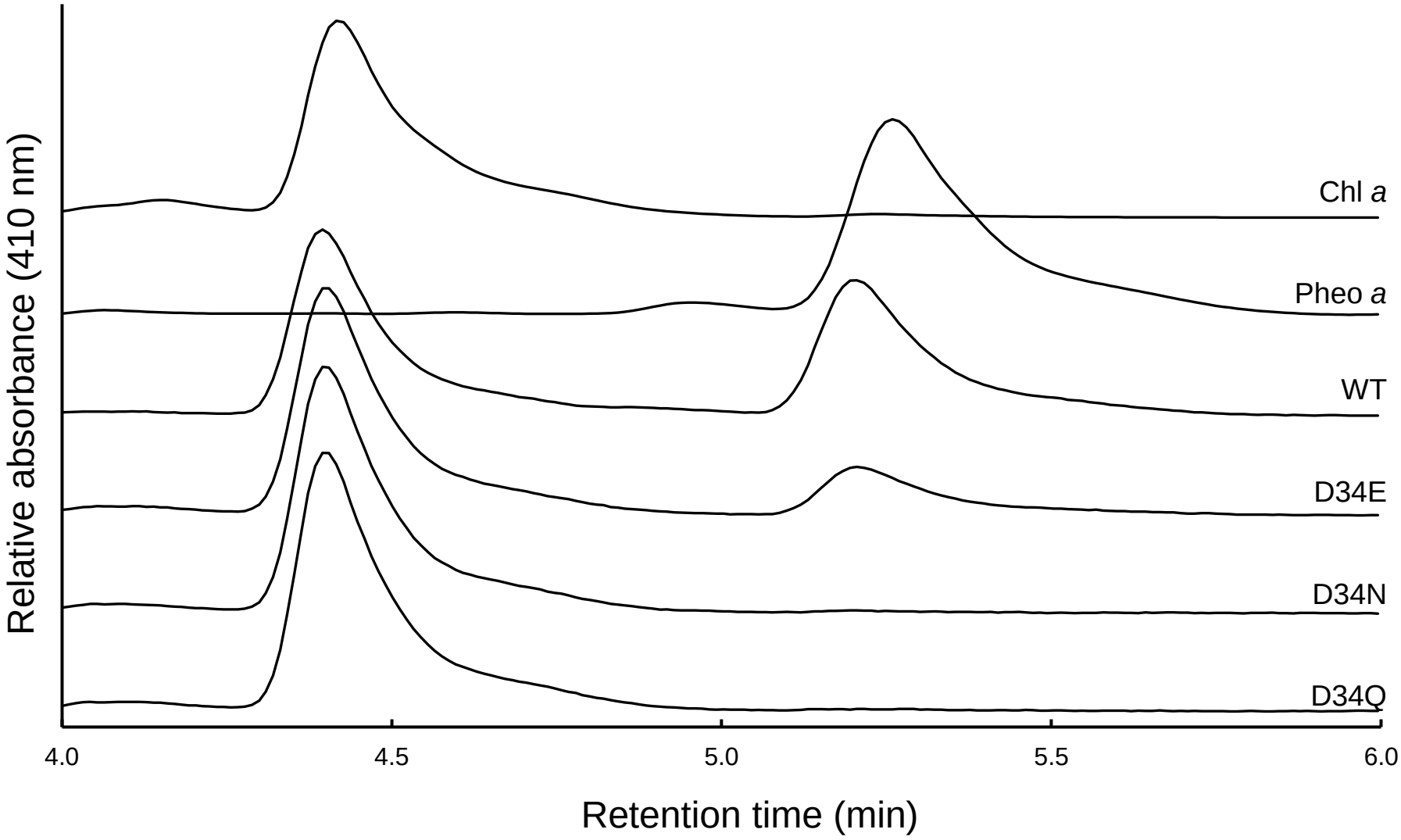
Relative absorbance (410 nm)
Chl a
Pheo a
WT
D34E
D34N
D34Q
4.0
4.5
5.0
5.5
6.0
Retention time (min)

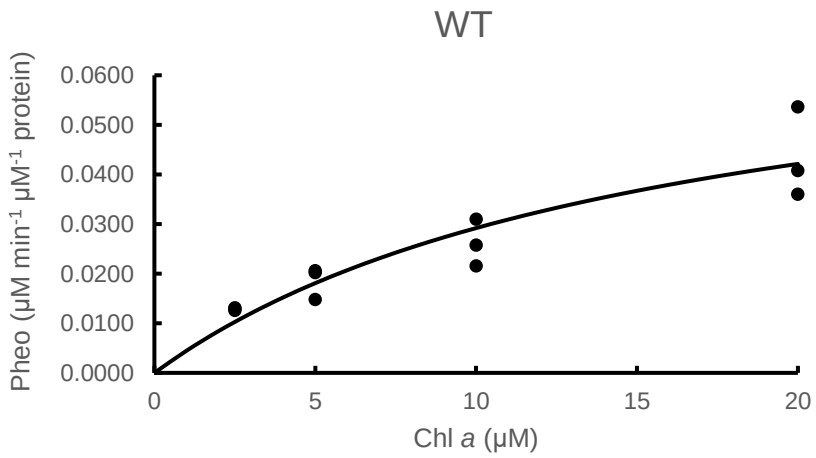
WT
Pheo (μM min-1 μM-1 protein)
0.0600
0.0500
0.0400
0.0300
0.0200
0.0100
0.0000
0
5
10
15
20
Chl a (μM)

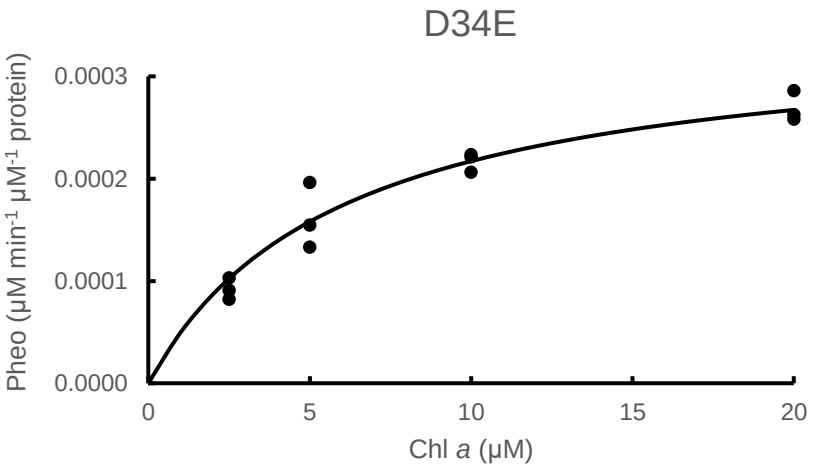
D34E
Pheo (μM min-1 μM-1 protein)
0.0003
0.0002
0.0001
0.0000
0
5
10
15
20
Chl a (μM)

(a)

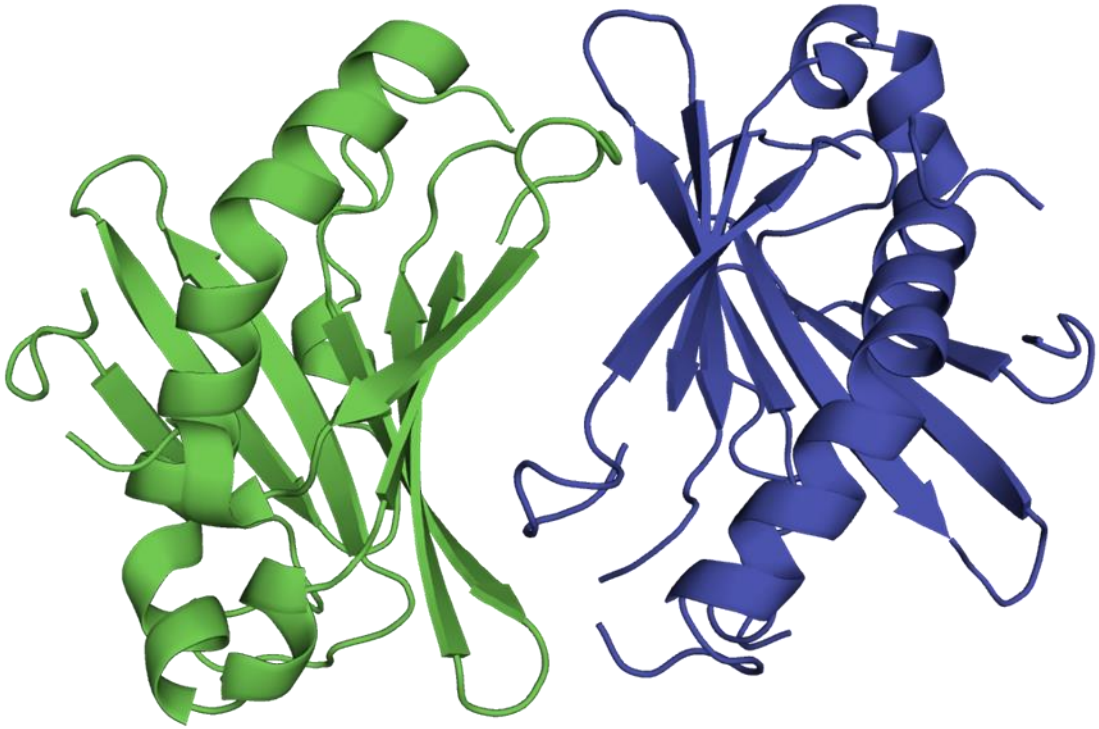

(b)

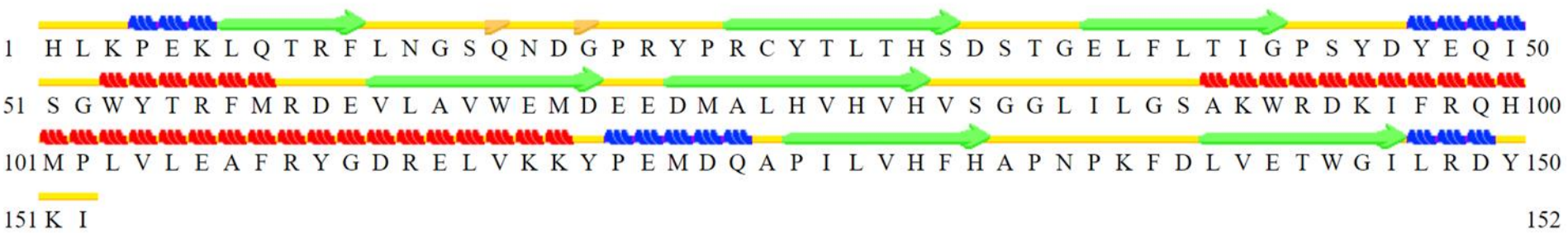
1 H L K P E K L Q T R F L N G S Q N D G P R Y P R C Y T L T H S D S T G E L F L T I G P S Y D Y E Q I 50
51 S G W Y T R F M R D E V L A V W E M D E E D M A L H V H V H V S G G L I L G S A K W R D K I F R Q H 100
101 M P L V L E A F R Y G D R E L V K K Y P E M D Q A P I L V H F H A P N P K F D L V E T W G I L R D Y 150
151 K I
152

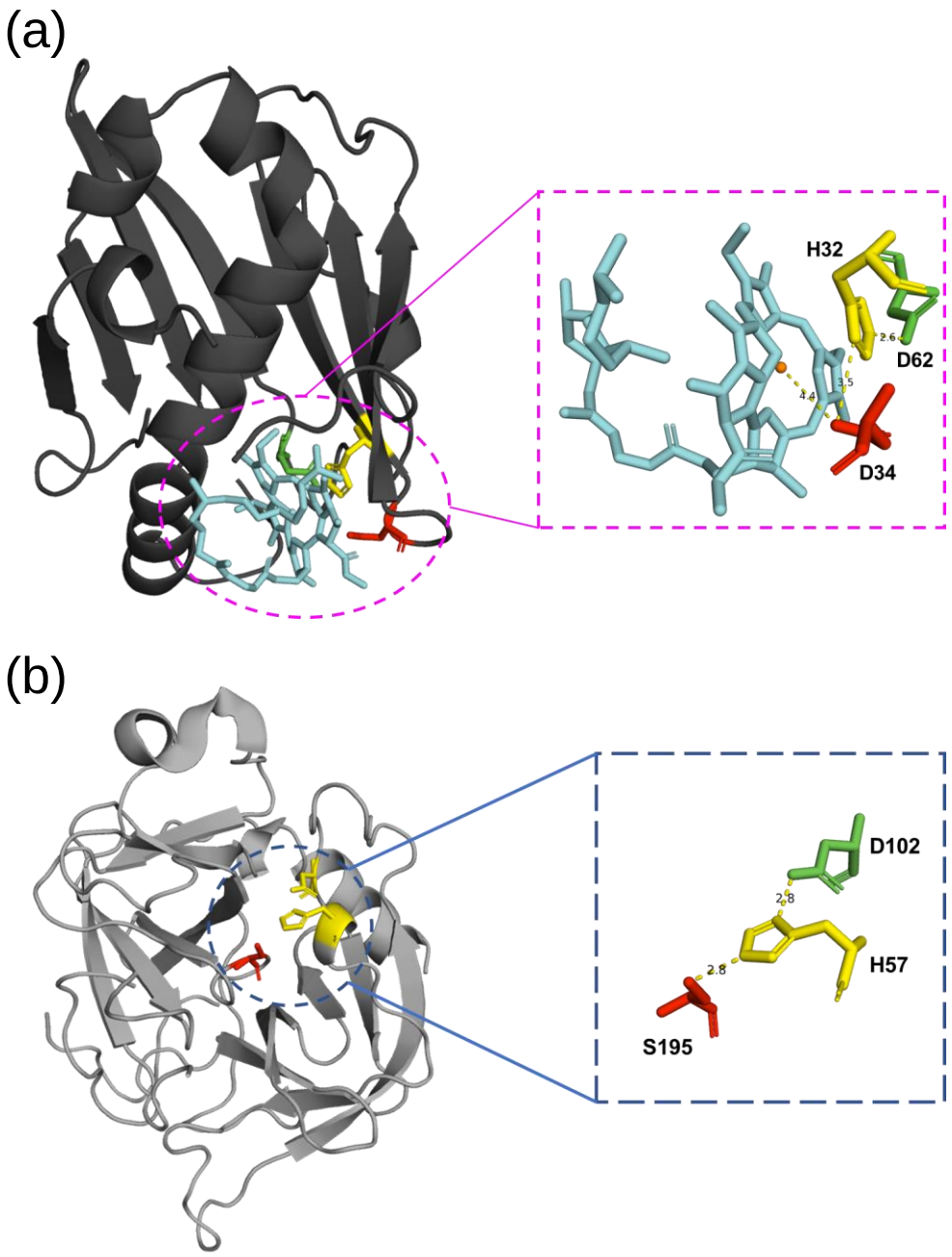
(a)
H32
D62
D34
2.6
3.5
4.4
(b)
D102
H57
S195
2.8
2.8

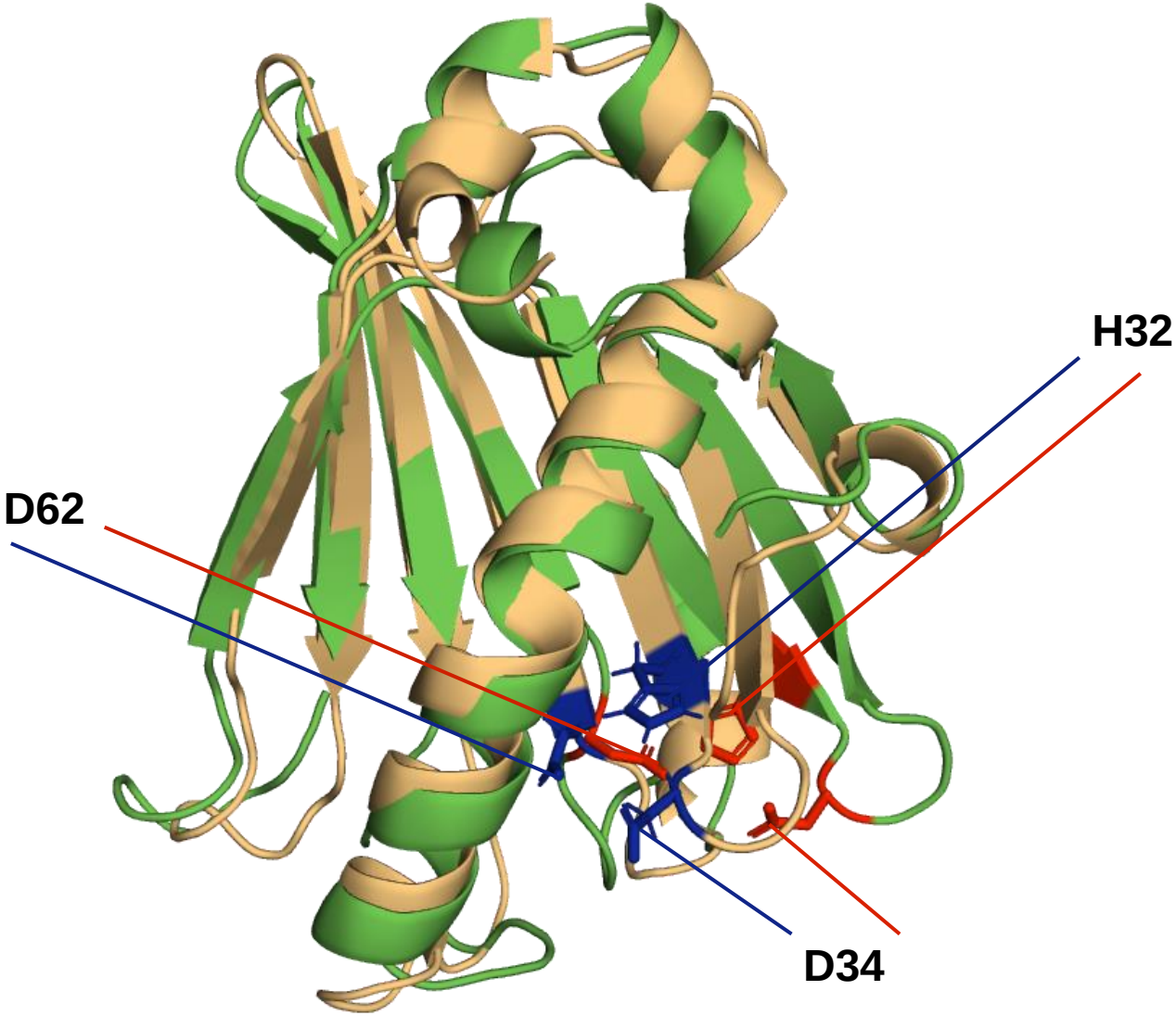
H32
D62
D34

Table S1: Primer sequences used for cloning and mutation

	Forward (5' → 3')	Reverse (5' → 3')
WT	AAGGAGATATACATATGGATCATCTGAAACCGGAG	GGTGGTGGTGCTCGATTTTGTAATCGCGCAGAATG
D34E	CCACAGCGAAAGCACCGGTGAACTGTTTCT	CGGTGCTTTCGCTGTGGGTCAGGGTATAGC
D34N	CCACAGCAATAGCACCGGTGAACTGTTTCT	CGGTGCTATTGCTGTGGGTCAGGGTATAGC
D34Q	CCACAGCCAGAGCACCGGTGAACTGTTTCT	CGGTGCTCTGGCTGTGGGTCAGGGTATAGC

(a)

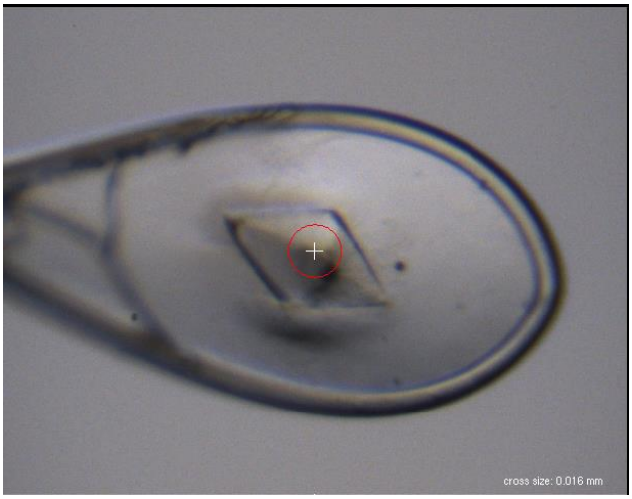

(b)

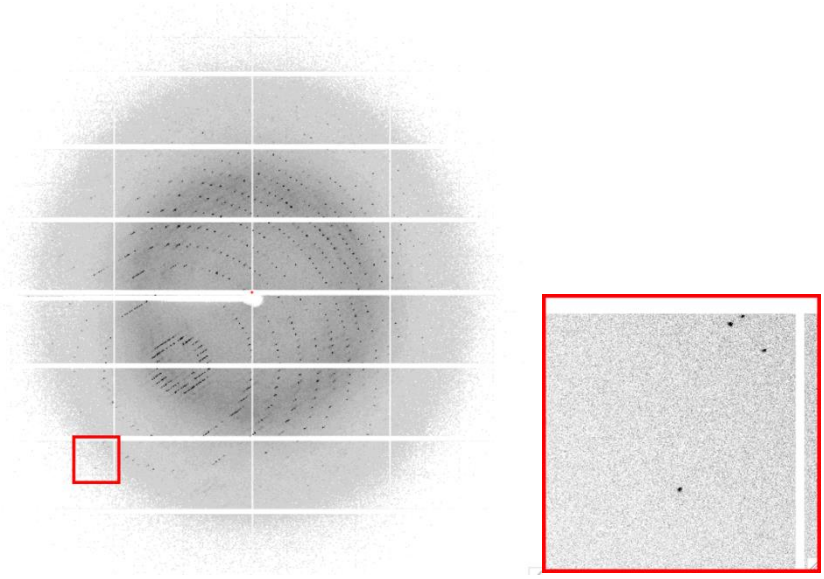

Figure S1 Photograph of AbSGR-h crystal and X-ray diffraction pattern. (a) The crystal was about 0.2 mm × 0.1 mm × 0.05 mm, and belongs to the space group $P6_122$ with cell dimensions of a=80.3 Å, b=80.3 Å, c=224.8 Å, β=120.0°. (b) X-ray experiments were performed at 100 K with a EIGER X16M detector (Dectris) on BL44XU beamline at SPring-8 (Harima, Hyogo, Japan). A whole image of the diffraction pattern (left) and a magnified view of the diffraction pattern (right). The crystal diffracted up to 1.6 Å resolution.